SpheroidOnADrop: A Modular Droplet Microfluidics Platform

Advanced Materials Technologies

ADVANCED MATERIALS TECHNOLOGIES
www.advmattechnol.com

RESEARCH ARTICLE OPEN ACCESS

Spheroid-On-A-Drop: A Modular Droplet Microfluidics Platform

A. Fergola[1] | V. Vighetto[1] | G. Mesiano[1] | A. Cosola[1] | S. L. Marasso[1,2] | M. Cocuzza[1,2] | C. F. Pirri[1] | L. Napione[1] | F. Frascella[1]

[1]Department of Applied Science and Technology (DISAT) – PolitoBIOMed Lab, Politecnico di Torino, Torino, Italy | [2]Consiglio Nazionale delle Ricerche, Istituto dei Materiali per l'Elettronica ed il Magnetismo (CNR IMEM), Parma, Italy

Correspondence: V. Vighetto (veronica.vighetto@polito.it)

Received: 7 January 2026 | **Revised:** 11 June 2026 | **Accepted:** 3 July 2026

Keywords: 3D tissue models | cell analysis | cell encapsulation | droplet-based microfluidics | high-throughput screening | hydrogel microparticles | photo-crosslinking

ABSTRACT

Droplet-based microfluidics offers a robust route to fabricate hydrogel microcarriers with high precision and reproducibility. Here, we present Spheroid-on-a-Drop, a pressure-driven microfluidic platform for generating monodisperse gelatin methacryloyl (GelMA) microgels for 3D cell encapsulation and spheroid culture. The device combines a flow-focusing junction for controlled droplet breakup with an upstream spiral microchannel used as a passive hydrodynamic conditioning module to improve suspension uniformity and cell spatial distribution prior to gelation. Operating parameters were systematically optimized to achieve stable droplet generation in the dripping regime and narrow size distributions. The resulting GelMA microgels showed high monodispersity, structural integrity, and tunable swelling behavior across media and temperature conditions; SEM imaging of lyophilized samples indicated a homogeneous internal morphology consistent with uniform crosslinking and high water content. As biological validation, A549 human lung carcinoma cells were encapsulated within GelMA microgels, showing high post-encapsulation viability and the formation of compact 3D spheroids during culture. Overall, Spheroid-on-a-Drop provides a reproducible and tunable method to produce biocompatible GelMA microgels for 3D tumor spheroid modeling and downstream applications in drug screening.

1 | Introduction

Droplet-based microfluidics (DBM) has emerged as one of the most powerful platforms for the generation of monodisperse biomaterial microgels, enabling precise control over their size, composition, and internal architecture [1, 2]. Recent advances have further expanded the capabilities of droplet microfluidics for biofabrication, single-cell analysis, and high-throughput screening applications, highlighting the increasing maturity and versatility of the field [3, 4]. Unlike traditional fabrication methods such as emulsion polymerization or mechanical stirring—often limited by broad size distributions, low reproducibility, and potential damage to biological components—DBM allows the formation of highly uniform droplets that serve as independent microreactors for the synthesis and crosslinking of hydrogels [5–7]. By exploiting controlled flow dynamics at the microscale, DBM systems provide reproducible conditions for polymerization, particle solidification, and cell encapsulation, making them an essential tool for applications in tissue engineering, drug delivery, and single-cell biology [8, 9].

Within DBM devices, each droplet constitutes a confined 3D microenvironment where physical, chemical, and biological cues can be finely tuned. This confinement mimics the microscale

organization of natural tissues, supporting cell viability, proliferation, and differentiation while ensuring uniform nutrient and oxygen diffusion [10–12]. The ability to modulate interfacial tension, flow rate ratios, and surfactant composition enables dynamic control over droplet morphology, leading to the fabrication of microgels with tailored porosity, stiffness, and degradation profiles. Furthermore, by integrating passive or active hydrodynamic modules—such as inertial focusing, acoustic manipulation, or Dean flow induction—DBM platforms can overcome Poissonian loading limitations, improving single-cell encapsulation efficiency and the spatial organization of cells within droplets [13–16].

Among the various biomaterials employed in DBM, gelatin methacryloyl (GelMA) has gained particular attention in applications involving tissue engineering scaffolds [17–19], drug-laden carriers [20], and electrochemical sensors [21] due to its biocompatibility and tunable physical characteristics. GelMA retains the arginine–glycine–aspartic acid (RGD) and matrix metalloproteinase (MMP)-sensitive sequences derived from native gelatin, promoting cell adhesion and remodeling of the surrounding hydrogel matrix [22, 23]. Its methacryloyl modification enables UV-initiated polymerization under mild conditions, allowing spatial and temporal control over crosslinking and the creation of diverse structures—from bulk hydrogels to microcapsules and microgels [24, 25]. These characteristics make GelMA ideally suited for droplet-based fabrication, where rapid polymerization and fine control of the prepolymer phase are required.

The integration of GelMA with DBM represents a significant advance in the design of cell-laden microgels and 3D tissue-like architectures. Such systems combine the precision of microfluidic flow control with the biological performance of GelMA, enabling the production of monodisperse, structurally stable, and biologically active microgels [26]. These microgels can function as modular building blocks for assembling larger constructs or as individual culture units for cell encapsulation and analysis at the microscale. Recent studies demonstrated that GelMA-based DBM systems support cell proliferation, matrix remodeling, and high encapsulation efficiency, establishing them as a cornerstone for next-generation biofabrication and regenerative medicine platforms [27].

Despite the wide adoption of droplet-based microfluidics for GelMA microgel fabrication, most reported platforms for 3D cell culture rely on architecturally complex or hybrid systems, rather than on GelMA-only microcarriers. Comprehensive reviews of microfluidic-assisted tissue engineering consistently show that GelMA is predominantly employed in combination with secondary materials (e.g., alginate, PEGDA, chitosan) or within core–shell, porous, or sacrificial architectures to achieve adequate mechanical stability, mass transport, or spatial compartmentalization [26, 28]. Representative examples include the one-step generation of core–shell GelMA microgels incorporating a methylcellulose core to promote cell aggregation and shield encapsulated cells from hydrodynamic stress, explicitly acknowledging the limitations of solid GelMA microgels for spheroid formation [29]. More recently, highly porous GelMA microspheres enabling spatially controlled coculture were achieved through aqueous two-phase system templating and alginate placeholders, followed by chelation-induced removal of the sacrificial phase, resulting in a multi-material, multi-step fabrication workflow [30].

While these strategies successfully enhance biological performance, they intrinsically couple cell behavior to additional materials, sacrificial phases, or hierarchical architectures, increasing system complexity and limiting reproducibility and scalability. In contrast, a systematic and quantitative characterization of GelMA-only droplet-based microfluidic systems, explicitly optimized for direct cell encapsulation and spheroid formation, remains largely unexplored. In particular, existing studies rarely establish quantitative correlations between droplet-generation hydrodynamics, early cell positioning within the droplet, and post-crosslinking microgel properties that ultimately govern spheroid uniformity and maturation.

Addressing this gap is essential to define robust design rules for minimal, single-material GelMA microcarriers, enabling reproducible 3D spheroid culture while preserving the intrinsic ECM-mimetic bioactivity, enzymatic degradability, and cell–matrix interactions of GelMA, without reliance on hybrid or sacrificial components.

In this work, we introduce *Spheroid-on-a-Drop*, a droplet-based microfluidic platform in which spheroid formation is initiated and spatially constrained at the level of individual droplets that are subsequently converted into hydrogel microgels. In practical terms, the term “on a drop” refers to the use of monodisperse droplets as both geometric templates and confined microenvironments, where the initial number and spatial distribution of cells are defined at the droplet stage and directly dictate downstream spheroid assembly.

The platform integrates a flow-focusing junction with an upstream spiral microchannel, used as a passive hydrodynamic conditioning module to improve suspension uniformity and cell spatial distribution prior to droplet formation. This design enables reproducible encapsulation under pressure-driven operation, followed by in situ UV crosslinking to yield GelMA microgels with well-defined size and morphology. The reliability of the system is demonstrated by the narrow microgel size distribution, predictable cell occupancy statistics, and reproducible spheroid formation across independent conditions. Specifically, quantitative analysis shows consistent encapsulation efficiency and a stable fraction of spheroid-forming microgels at day 5 for different initial cell concentrations.

Tunability is achieved through straightforward control of operational parameters, including flow conditions and input cell density, allowing modulation of microgel size, initial cell number per microgel, and the probability of spheroid formation. Together, these features establish *Spheroid-on-a-Drop* as a reliable and tunable platform for generating hydrogel-based microcarriers that support controlled 3D tumor spheroid culture, with potential applications in tissue modeling and drug screening.

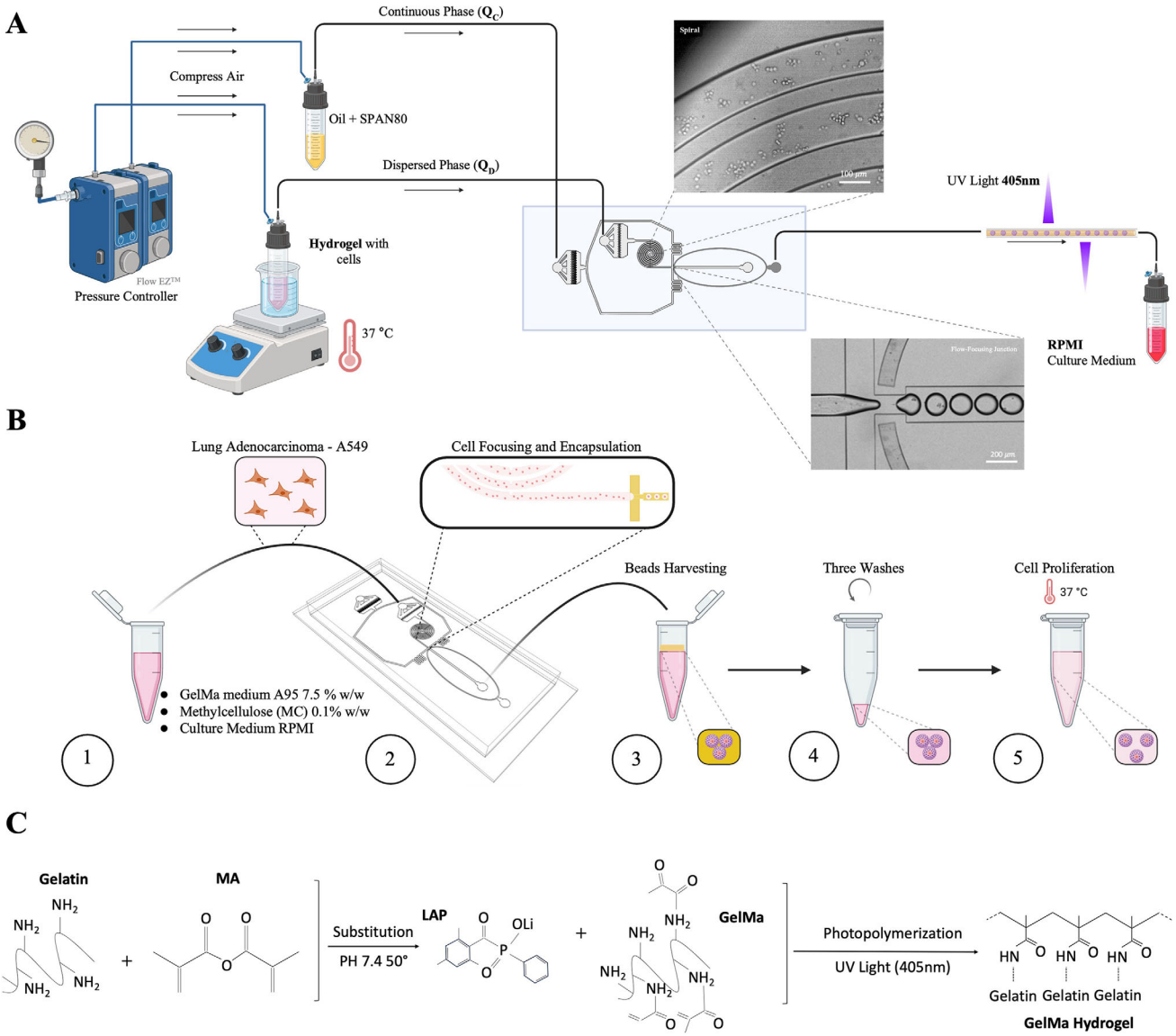

FIGURE 1 | Schematic representation of the droplet-based microfluidic platform for GelMA microgel generation, post-processing, and chemical structure. (A) Workflow of the droplet microfluidic setup integrating a pressure-driven control module (Flow EZ, Fluigent) for precise flow regulation. The GelMA precursor solution was maintained on a hot plate to prevent premature gelation at room temperature and to preserve physiological conditions for cell handling. Before reaching the droplet generation unit, the dispersed phase flowed through a microfluidic spiral channel used as a passive hydrodynamic conditioning module to promote homogeneous cell distribution. Droplet formation occurred at the flow-focusing junction, where the aqueous and oil phases intersected under laminar flow. Photopolymerization of the GelMA droplets was performed at the outlet using a dual perpendicular UV illumination system (405 nm). (B) Post-processing workflow for GelMA microgels, including collection in culture medium, triple washing to remove the oil phase, and incubation at 37°C for downstream analyses. (C) Schematic representation of GelMA synthesis and photopolymerization. Gelatin reacts with methacrylic anhydride to yield GelMA, which is subsequently crosslinked under 405 nm UV exposure to form a covalently bonded hydrogel network. Scale bars: 200 μm.

2 | Results

2.1 | Design and Fabrication of the Droplet Microfluidic Device

A droplet-based microfluidic device was designed and fabricated to generate GelMA microgels for cell encapsulation (Figure 1A). The platform combines a flow-focusing droplet generator with an upstream spiral microchannel (Figure S1), included as a passive hydrodynamic conditioning module to improve suspension homogenization and cell spatial distribution prior to gelation.

Droplet generation occurred at the flow-focusing junction, where the shear stress exerted by the continuous oil phase induced the breakup of the aqueous GelMA phase into uniform droplets, forming a stable water-in-oil (w/o) emulsion. Flow control was achieved via a Fluigent pressure-based module, allowing precise adjustment of the inlet pressures and, consequently, the droplet diameter and production frequency. Immediately after formation,

the droplets were photopolymerized at the outlet using a dual 405 nm LED illumination system oriented perpendicularly to the outlet tubing, providing uniform light exposure and minimizing potential photo-induced stress on encapsulated cells. Photopolymerization was therefore performed on-chip within a few seconds after droplet breakup and prior to collection, ensuring homogeneous gelation throughout the droplet volume while minimizing cell sedimentation and redistribution before crosslinking. This setup ensured homogeneous crosslinking of the GelMA matrix, resulting in monodisperse microgels with consistent size and morphology. Following collection, the microgels were purified by successive washing and centrifugation steps to remove residual oil and surfactant (Figure 1B). The resulting GelMA microgels were then used either as a cellular hydrogel carriers or as 3D scaffolds for cell encapsulation and culture. The synthetic route of GelMA and the mechanism of photopolymerization under UV light are shown in Figure 1C, depicting the methacrylation of gelatin with methacrylic anhydride and the subsequent crosslinking of methacryloyl groups upon 405 nm irradiation, forming the final hydrogel network. Further details on device fabrication and operational parameters are provided in the Materials and Methods section (see Section 5.2 "Microfluidic Chip Fabrication" and 5.5 "Microgels Generation").

2.1.1 | Hydraulic Resistance Network and Equivalent Circuit Model

To provide a compact analytical description of the pressure-driven operation of the microfluidic platform, the device was mapped onto an equivalent electrical circuit, where pressure drop ΔP and volumetric flow rate Q are analogous to voltage and current, respectively, and each microfluidic channel segment is represented as a hydraulic resistance $R_h = \Delta P/Q$ (Figure 2).

In this representation, the oil and GelMA inlet lines are modeled as resistive elements connected to the flow-focusing junction, while the upstream conditioning modules—comprising the serpentine and spiral microchannels as well as the connecting straight segments—are represented as resistances connected in series along the corresponding flow paths. The outlet is modeled as a reference pressure node, consistent with the pressure-driven experimental setup.

Hydraulic resistances were estimated assuming fully developed laminar flow in rectangular microchannels using the standard analytical expression corrected for finite aspect ratio [31]:

$$R_h = \frac{12\mu L}{w_{eff} h^3 \left(1 - 0.63\frac{h}{w_{eff}}\right)} \quad (1)$$

where μ is the dynamic viscosity of the fluid, L is the channel length, h is the channel height, and w_{eff} is an effective channel width. For channel segments with mild width variations, w_{eff} was approximated as the arithmetic mean of the minimum and maximum widths along the segment:

$$w_{eff} = \frac{w_{min} + w_{max}}{2} \quad (2)$$

This circuit-based formulation provides a simplified yet physically consistent framework to relate the imposed inlet pressures to the resulting flow rates at the flow-focusing junction, enabling rational confirmation of stable operating conditions and facilitating comparison across different pressure configurations without resorting to full numerical simulations.

2.1.2 | Microfluidic Spiral as a Pre-Conditioning Model for Cell Distribution Prior Encapsulation

To quantitatively assess the effect of the spiral microchannel on cell spatial distribution prior to encapsulation, a dedicated brightfield videomicroscopy experiment was performed comparing no-spiral reference configuration (Figure 3A) with the spiral preconditioning condition (Figure 3B) under identical flow conditions (P_D = 60 mbar; GelMA 7.5% w/v + MC 0.1% w/v; 37°C). A seeding density of 8×10^6 A549 cells/mL was employed in this characterisation experiment, as this concentration amplifies local heterogeneity signals to levels reliably detectable by brightfield intensity analysis at 5× magnification, while preserving the hydrodynamic regime of the actual encapsulation experiments, in which flow conditions are governed by the GelMA–MC matrix rather than by cell concentration (see Section 5.8 for experimental details and Section S3 for full computational details of the image analysis pipeline). Cell distribution uniformity was quantified frame-by-frame through the coefficient of variation (CV) of a local intensity variance proxy computed within a binary channel mask, over N = 310 frames (no-spiral) and N = 204–244 frames per loop (spiral). The CV provides a dimensionless, acquisition-independent index of spatial heterogeneity within the channel cross-section at each time point; its temporal stability across the acquisition window (Figure 3C) confirms that both conditions represent steady-state hydrodynamic regimes rather than transient phenomena, and that the measured distributions are not attributable to temporal fluctuations in cell loading or flow.

Under no-spiral conditions, the mean CV was 122.4 ± 11.3% (Figure 3D,E), indicating pronounced spatial heterogeneity. The normalised axial density profile, computed as the mean ± SEM of N = 310 frames per spatial bin, revealed a non-uniform distribution along the channel axis, with elevated cell density signal in the inlet region and a progressive depletion toward the outlet (Figure 3H), consistent with gravitational sedimentation and aggregate formation in the absence of hydrodynamic redistribution.

In contrast, cells flowing through the spiral microchannel exhibited markedly more uniform spatial distributions across all three monitored loop positions, with mean CV values of 43.3 ± 3.7% (outlet loop), 38.6 ± 3.4% (intermediate loop), and 33.4 ± 4.1% (inlet loop) (Figure 3D–F). All pairwise comparisons with the no-spiral condition were statistically significant (Mann–Whitney U test, two-sided: $p = 1.65 \times 10^{-83}$, 4.22×10^{-82}, and 6.51×10^{-91} for the outlet, intermediate, and inlet loops, respectively; Figure 3D,E). The empirical cumulative distribution functions of per-frame CV showed complete non-overlapping separation between the no-spiral condition and all spiral loops across the entire CV range (Figure 3G), providing distribution-level

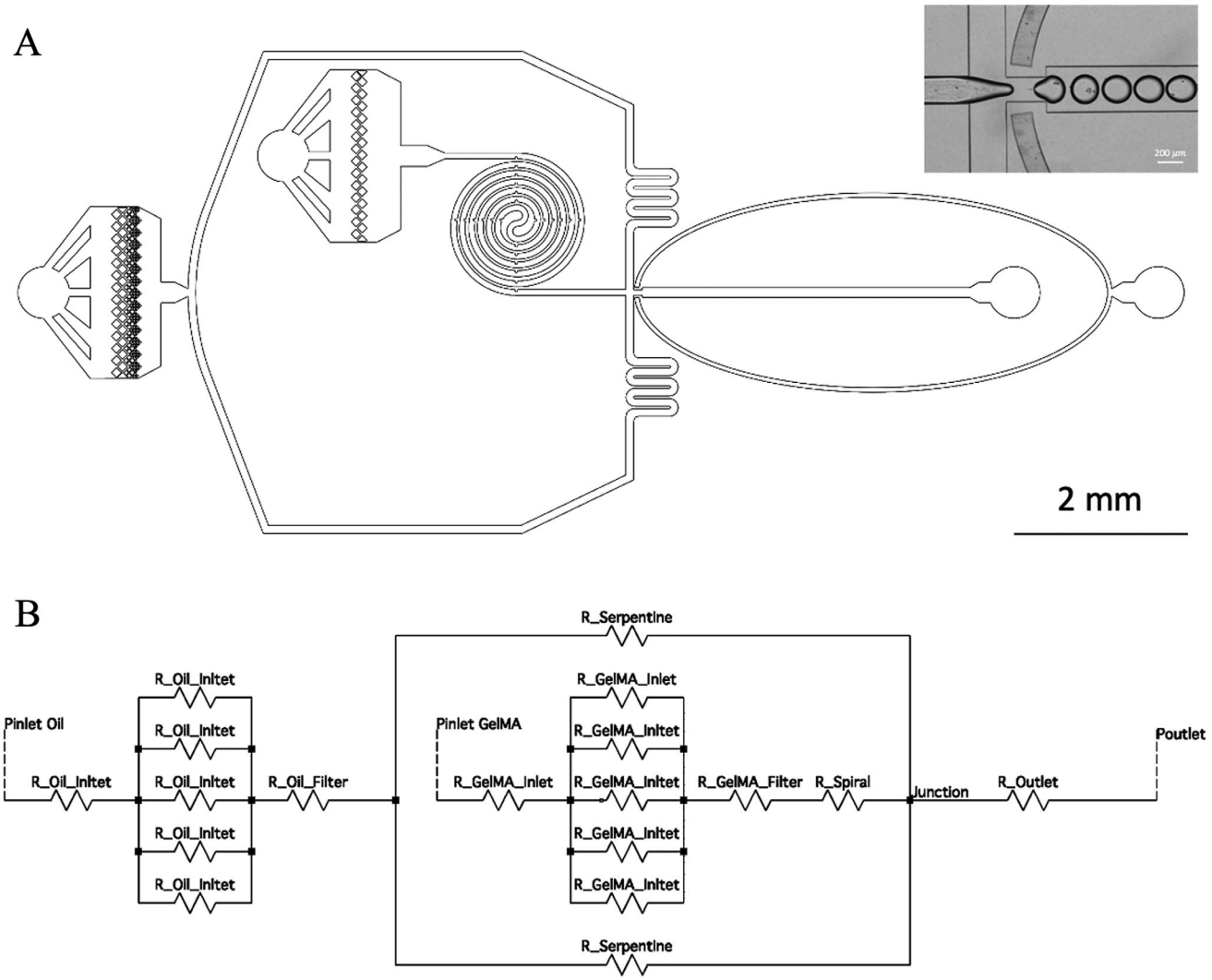

FIGURE 2 | Device layout and equivalent hydraulic–electrical circuit representation. (A) Two-dimensional CAD layout of the droplet-based microfluidic device. The inset shows optical microscopy images of the flow-focusing junction during A549 cell encapsulation, highlighting stable droplet formation under pressure-driven operation. (B) Equivalent electrical circuit representation of the pressure-driven microfluidic device. Microfluidic channel segments are modeled as hydraulic resistances ($R_h = \Delta P/Q$). The oil and GelMA inlet networks are represented by resistive elements feeding the flow-focusing junction, while upstream conditioning modules (serpentine and spiral channels) are modeled as resistances connected in series along the main flow paths. The outlet is treated as a reference pressure node, consistent with the experimental pressure-controlled operation.

evidence of the preconditioning effect that is independent of any single summary statistic. The fold reduction in median CV ranged from 2.8× at the outlet loop to 3.7× at the inlet loop (Figure 3D), with the progressive improvement along the spiral path consistent with a cumulative passive conditioning mechanism rather than an abrupt hydrodynamic transition.

Taken together, these results demonstrate that the spiral microchannel reduces cell distribution heterogeneity by 2.8–3.7-fold relative to the no-spiral reference, with an effect that is statistically robust, temporally stable, and spatially consistent across the full length of the spiral. These findings support the interpretation of the spiral as a passive preconditioning module that improves suspension uniformity prior to the flow-focusing junction, thereby providing more controlled initial conditions for droplet-based cell encapsulation.

2.2 | Optimization of the Parameters in the Droplet Microfluidic Device

Optimization of the droplet-based microfluidic platform was carried out to determine the operating conditions that ensured stable and monodisperse GelMA microgels.

Among the tested variables, the pressures applied to the dispersed and continuous phases, together with the GelMA concentration, were identified as the key parameters influencing droplet size and formation stability (Figure 4A,B).

Systematic tests demonstrated that both droplet diameter and generation frequency were strongly dependent on the pressure ratio (P_D/P_C) between the two phases, consistent with a shear-driven breakup mechanism typical of flow-focusing geometries.

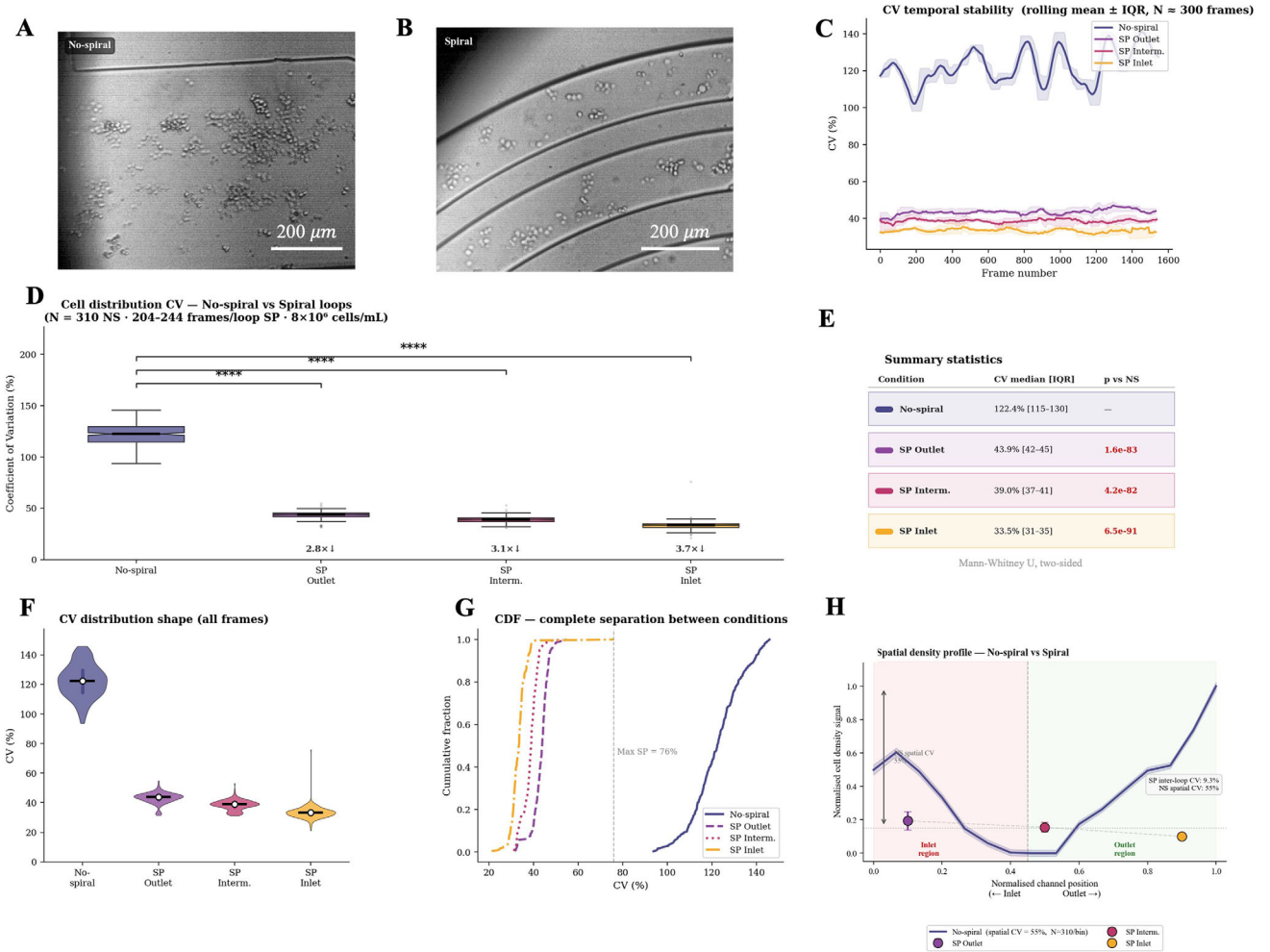

FIGURE 3 | Quantitative assessment of spiral microchannel preconditioning on A549 cell spatial distribution prior to droplet encapsulation (8×10^6 cells/mL; P_D = 60 mbar; GelMA 7.5% w/v + MC 0.1% w/v). (A) Representative brightfield micrograph of A549 cells in the no-spiral reference configuration, showing pronounced cell clustering at the channel inlet. Scale bar: 200 μm. (B) Representative brightfield micrograph of A549 cells flowing through the spiral microchannel, showing uniform distribution across the channel cross-section. Scale bar: 200 μm. (C) Temporal evolution of the coefficient of variation (CV) of the local intensity variance signal over N ≈ 300 consecutive frames per condition; lines represent rolling means (window = 15 frames) and shaded bands indicate the interquartile range, confirming steady-state distribution for all conditions. (D) Notched boxplots of per-frame CV for the no-spiral condition and the three spiral loops (outlet, intermediate, inlet); brackets denote Mann–Whitney U test significance (**** $p < 0.0001$; individual p-values: $p = 1.65 \times 10^{-83}$, 4.22×10^{-82}, and 6.51×10^{-91} for outlet, intermediate, and inlet loops vs. no-spiral, respectively; N = 310 frames, no-spiral; N = 210, 204, and 244 frames for outlet, intermediate, and inlet loops, respectively). Annotated values below each box report the fold reduction in median CV relative to no-spiral. (E) Summary statistics table reporting the CV median, interquartile range, and Mann–Whitney U p-value versus the no-spiral reference for each condition. (F) Violin plots of per-frame CV distributions; white circles indicate medians and thick bars indicate interquartile ranges. (G) Empirical cumulative distribution functions (CDFs) of per-frame CV, showing complete non-overlapping separation between the no-spiral and all spiral loop conditions; the dashed vertical line marks the maximum CV observed across spiral loops. (H) Normalised spatial density profiles: the no-spiral line represents the mean ± SEM of N = 310 frames per spatial bin; spiral loop symbols represent per-loop mean signals (N = 210, 204, 244 frames for outlet, intermediate, and inlet, respectively). Shaded regions delimit the inlet and outlet zones of the no-spiral channel. The no-spiral profile exhibits marked axial heterogeneity, while all spiral loops display a near-flat profile consistent with uniform cell distribution.

Under optimized conditions, the device reproducibly generated uniform GelMA droplets with a narrow size distribution and stable production rate. In addition, the swelling behavior of photocrosslinked GelMA microgels was later evaluated in different aqueous environments to assess network stability and solvent responsiveness (Section 2.2.2). Together, these results defined the working parameters for obtaining hydrogel microcarriers suitable for cell encapsulation and biological downstream assays. Details of pressure control, droplet imaging, and quantitative analysis are provided in Materials and Methods (Section 5.5 "Microgels Characterization" and Section 5.12 "Statistics").

2.2.1 | Effect of Flow Rates on Droplet Generation and Size

To investigate the impact of inlet pressures on droplet formation dynamics, the ratio between the dispersed (P_D) and continuous (P_C) phases was varied across five configurations: 40/50, 60/70,

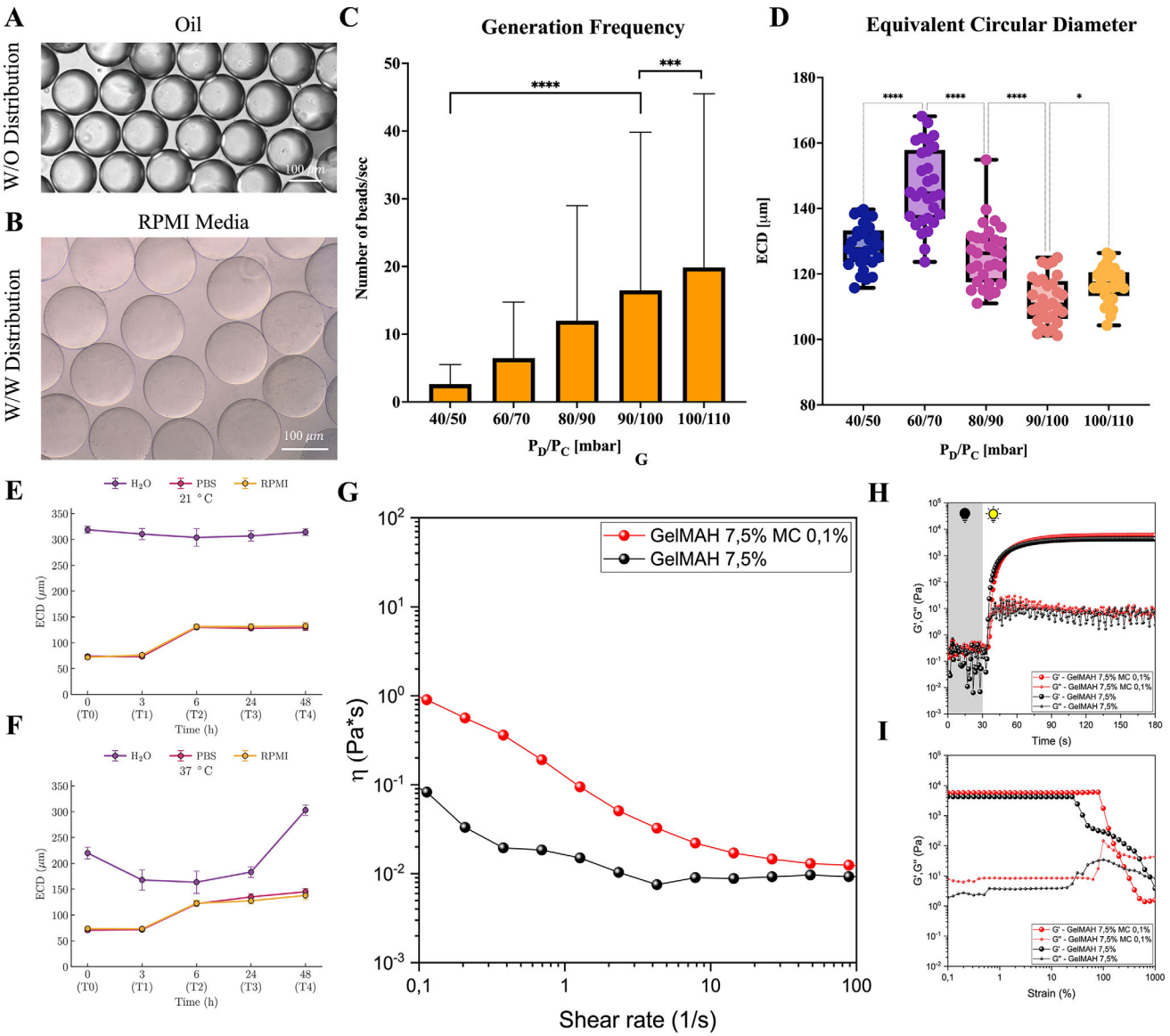

FIGURE 4 | Characterization and optimization of GelMA microgel generation and swelling behavior in the droplet-based microfluidic platform. (A) Optical micrograph of GelMA microgels immediately after formation in the oil phase, showing uniform spherical morphology and high monodispersity. (B) Optical image of GelMA microgels after transfer into the aqueous phase, highlighting their structural integrity and stability following photopolymerization and purification. (C) Quantification of droplet generation frequency (beads s^{-1}) at different pressure configurations of the dispersed and continuous phases, demonstrating a significant increase in production rate with higher applied pressures. (D) Variation of the equivalent circular diameter (ECD) of GelMA microgels under the same pressure conditions, showing a size reduction with increasing pressure from the 60/70 mbar configuration onward, associated with enhanced shear forces at the flow-focusing junction. (E) Swelling behavior of GelMA microgels at 21°C in different media (distilled water, PBS, and RPMI), indicating minimal dimensional changes in pure water and moderate expansion in ionic environments. (F) Swelling behavior of GelMA microgels at 37°C under the same media conditions, revealing temperature-induced volume fluctuations consistent with thermal relaxation of the hydrogel network. (G) Steady-shear flow curves (rotational viscosity η versus shear rate, 0.1–100 s^{-1}) of the uncured precursors GelMA A95 7.5% w/v (black) and GelMA A95 7.5% w/v + MC 0.1% w/v (red), measured at 25°C, showing shear-thinning behaviour and a marked increase in low-shear viscosity upon MC addition. (H) Real-time photorheology at 37°C: evolution of the storage (G′) and loss (G″) moduli of the two formulations during 405 nm irradiation (light switched on after a 30 s equilibration period), showing rapid network formation and essentially unchanged crosslinking kinetics upon MC addition. (I) Amplitude sweep (G′, G″ versus strain) on the crosslinked hydrogels at 37°C, showing a well-defined linear viscoelastic region with G′ > G″. Measurements were performed in triplicate. Corresponding 25°C photorheology and amplitude-sweep data are reported in Figure S5. Scale bars: 100 μm.

80/90, 90/100, and 100/110 mbar, while maintaining the GelMA concentration constant at 7.5 % w/v.

As shown in Figure 4C, the generation frequency increased proportionally with the applied pressures, rising from 4.6 ± 0.57 beads s^{-1} at 40/50 mbar to 38 ± 1.73 beads s^{-1} at 100/110 mbar. Time-lapse acquisitions (60 loops at 60.2 fps) confirmed a stable dripping regime throughout all tested conditions.

Statistical analysis (one-way ANOVA) confirmed a significant influence of pressure on droplet generation rate (****$p < 0.0001$ for the first four groups; ***$p = 0.0002$ between 90/100 and 100/110 mbar).

A similar dependence was observed for droplet size (Figure 4D). From the 60/70 mbar configuration onward, the equivalent circular diameter (ECD) decreased with increasing flow rates, from 146.53 ± 11.94 µm at 60/70 mbar to 116.86 ± 5.34 µm at 100/110 mbar; the lowest-pressure configuration (40/50 mbar) yielded intermediate droplets of 128.42 ± 6.59 µm. The coefficient of variation (CV) of the equivalent circular diameter confirmed high monodispersity across all tested pressure configurations: 5.1% at 40/50 mbar, 8.2% at 60/70 mbar, 7.4% at 80/90 mbar, 6.4% at 90/100 mbar, and 4.6% at 100/110 mbar (N = 30 droplets per condition, three independent replicates (Section 5.11), consistent with stable dripping-regime droplet generation throughout the tested pressure range. At higher pressures, the reduction in diameter plateaued, suggesting the onset of a dripping-to-jetting transition where further increases in flow rate produced only minor variations ($p = 0.0383$).

Among the tested configurations, 60/70 mbar was selected as the optimized operating condition, since it produced monodisperse GelMA droplets of relatively large diameter—a desirable feature for subsequent cell encapsulation and proliferation assays, where larger internal volume improves nutrient diffusion and cell viability within the microgels. Experimental details, imaging protocols, and statistical procedures are reported in Materials and Methods (Section 5.5 and 5.12).

2.2.2 | Swelling Behavior of Hydrogel-Based Microcarriers

The swelling behaviour of GelMA microgels was evaluated to quantify their responsiveness to solvent composition and temperature (Figure 4E,F).

Microgels were incubated at 21°C and 37°C in three different media—distilled water, phosphate-buffered saline (PBS), and cell culture medium, i.e., RPMI culture medium—representing environments with distinct osmotic and ionic strengths. For each condition, the equivalent circular diameter (ECD) of the beads was monitored at T0 (0 h), T1 (3 h), T2 (6 h), T3 (24 h), and T4 (48 h).

At 21°C, microgels in distilled water maintained a nearly constant size (310.6 ± 4.2 µm) throughout 48 h, indicating negligible dimensional variation. In PBS and RPMI, an initial shrinkage was followed by progressive swelling, with ECD increasing from 73.6 ± 3.5 µm to 129.9 ± 4.1 µm in PBS and 71.8 ± 3.6 µm to 131.2 ± 4.9 µm in RPMI within 6 h.

At 37°C, the same trend persisted, though with slightly larger equilibrium sizes (144.9 ± 6.3 µm in PBS; 137.8 ± 7.9 µm in RPMI after 48 h). Conversely, in distilled water, microgels displayed a biphasic behaviour: a transient contraction between 0 h and 3 h (from 219.9 ± 11.3 µm to 167.8 ± 19.8 µm) followed by reswelling to 302.9 ± 10.0 µm at 48 h.

Overall, GelMA microgels exhibited solvent- and temperature-dependent dimensional variation while preserving their overall structural stability across all experimental conditions (for further details, see Section 3.1 "Optimization of the Parameters in the Droplet Microfluidic Device"). Experimental procedures for image acquisition and statistical analysis are detailed in Materials and Methods (Section 5.5 and 5.12).

2.2.3 | Rheological Behaviour of the GelMA–MC Precursor

The rheological properties of the dispersed phase were characterised to assess the contribution of methylcellulose (MC) to the formulation and its compatibility with the photocrosslinking step. Steady-shear flow measurements of the uncured precursors (Figure 4G) showed that both GelMA A95 7.5% w/v and GelMA A95 7.5% w/v + MC 0.1% w/v exhibited shear-thinning behaviour across the full range investigated (0.1–100 s^{-1}). The addition of MC produced a pronounced increase in low-shear viscosity — from ≈0.08 to ≈0.9 Pa·s at 0.1 s^{-1} — while at the upper end of the measured range (≥10 s^{-1}) the two curves converged to comparable values (≈0.01 Pa·s), indicating that the MC contribution is most pronounced under quasi-static, low-shear conditions and progressively vanishes as the shear rate increases.

The photoreactivity of the formulations was assessed by real-time photorheology at 37°C (Figure 4H; corresponding 25°C data in Figure S5). Upon 405 nm irradiation, both formulations underwent a rapid increase in storage modulus (G′), reaching a plateau on the order of 10^4 Pa, indicative of network formation. The incorporation of MC introduced only a marginal delay in the onset of crosslinking (≈1 s) and left the curing rate, estimated from the slope of the G′ curve, essentially unchanged, demonstrating that MC does not interfere with the photopolymerisation kinetics of GelMA. Amplitude sweeps on the crosslinked hydrogels at 37°C (Figure 4I; corresponding 25°C data in Figure S5) showed a well-defined linear viscoelastic region with G′ > G″ and a G′ plateau on the order of 10^4 Pa, consistent with a mechanically stable, covalently crosslinked network; a slight extension of the linear viscoelastic region was observed upon MC addition.

2.2.4 | SEM Characterization of Microgels

To investigate the morphology and microstructural organization of the GelMA microgels generated through the droplet-based microfluidic platform, freeze-dried samples were analyzed by

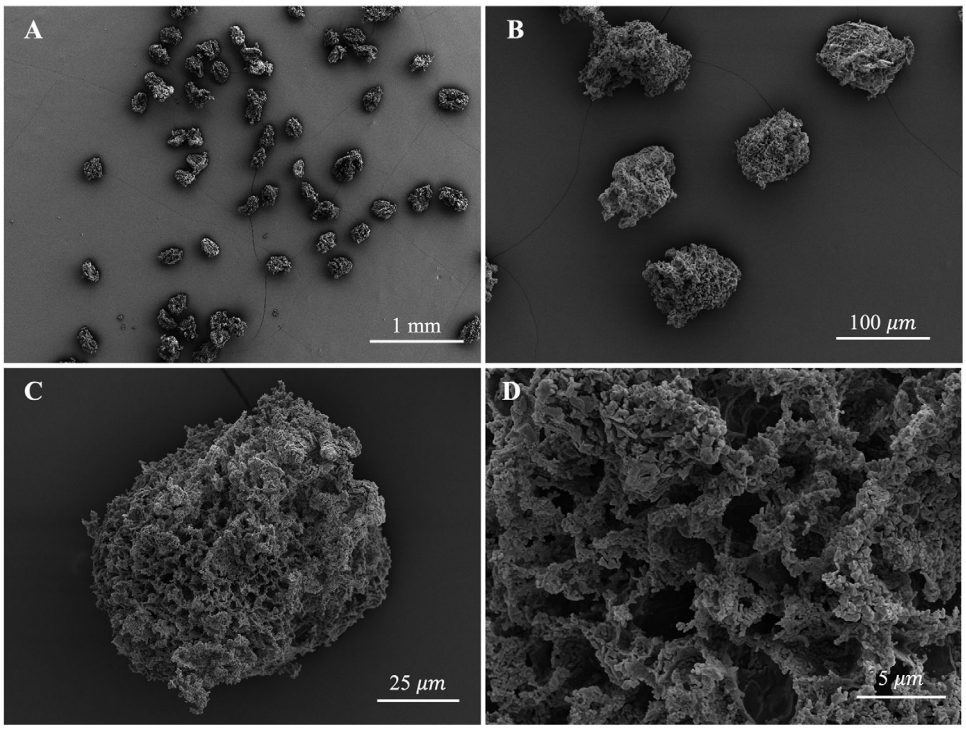

FIGURE 5 | SEM characterization of freeze-dried GelMA microgels generated by droplet-based microfluidics. (A) Low-magnification SEM image showing the overall morphology and spatial distribution of lyophilized GelMA microgels after rapid freezing in liquid nitrogen and freeze-drying. (B) Intermediate-magnification image highlighting the irregular external morphology and porous surface structure of individual microgels. (C) High-magnification view of a representative microgel showing the sponge-like internal organization composed of interconnected pores and polymeric lamellae. (D) Detailed visualization of the internal porous microarchitecture, revealing an open interconnected network generated by ice crystal templating and solvent sublimation during lyophilization. Scale bars: (A) 1 mm, (B) 100 μm, (C) 25 μm, (D) 5 μm.

scanning electron microscopy (SEM) (Figure 5). The analyzed microgels were produced under the optimized flow-focusing conditions described in Section 2.2.1 and subsequently subjected to rapid cryogenic freezing followed by lyophilization prior to imaging.

At low magnification (Figure 5A), the lyophilized microgels appeared as discrete collapsed structures with heterogeneous external morphologies and dimensions in the sub-millimetric range. Unlike the spherical hydrated morphology observed immediately after production in aqueous media (Section 2.2.1, Figure 4A,B), the dehydrated particles exhibited partial volumetric collapse and surface roughening induced by solvent sublimation during freeze-drying.

Higher magnification imaging (Figure 5B,C) revealed sponge-like particles characterized by interconnected cavities, irregular lamellar walls, and highly corrugated surfaces extending throughout the particle volume. This morphology is consistent with the high water content and swelling capability previously observed during the swelling analysis reported in Section 2.2.2, where GelMA microgels displayed substantial solvent-dependent dimensional variations.

At the highest magnification (Figure 5D), the internal microarchitecture consisted of an open porous network composed of interconnected polymeric sheets and micron-scale voids generated during ice crystal formation and subsequent sublimation. The absence of large phase-separated regions or macroscopic fractures suggests homogeneous photocrosslinking throughout the droplet volume during the UV polymerization process described in Section 2.1.

Overall, SEM analysis confirmed that the combination of droplet microfluidics, photocrosslinking, and freeze-drying produced structurally stable GelMA-derived porous microstructures while preserving the overall integrity of the microgels after dehydration.

2.3 | GelMA Microgels as 3D Microcarriers for Cell Cultures

Following optimization of the microfluidic device (Figure S2), a biological validation was conducted to assess the cytocompatibility of the encapsulation process and the capacity of GelMA microgels to support three-dimensional spheroid formation over extended culture periods.

Human lung carcinoma A549 cells were resuspended in GelMA prepolymer solutions at three initial concentrations — 500 000, 750 000, and 8×10^6 cells/mL — according to the procedures detailed in Section 5.8. The resulting cell–GelMA suspensions were processed under optimized microfluidic flow conditions, photopolymerized in situ, and cultured for up to 5 days in complete RPMI 1640 medium.

Cell viability at Day 5 was confirmed by LIVE/DEAD fluorescence imaging of the 500k cells/mL condition (Figure 6F). Predominant

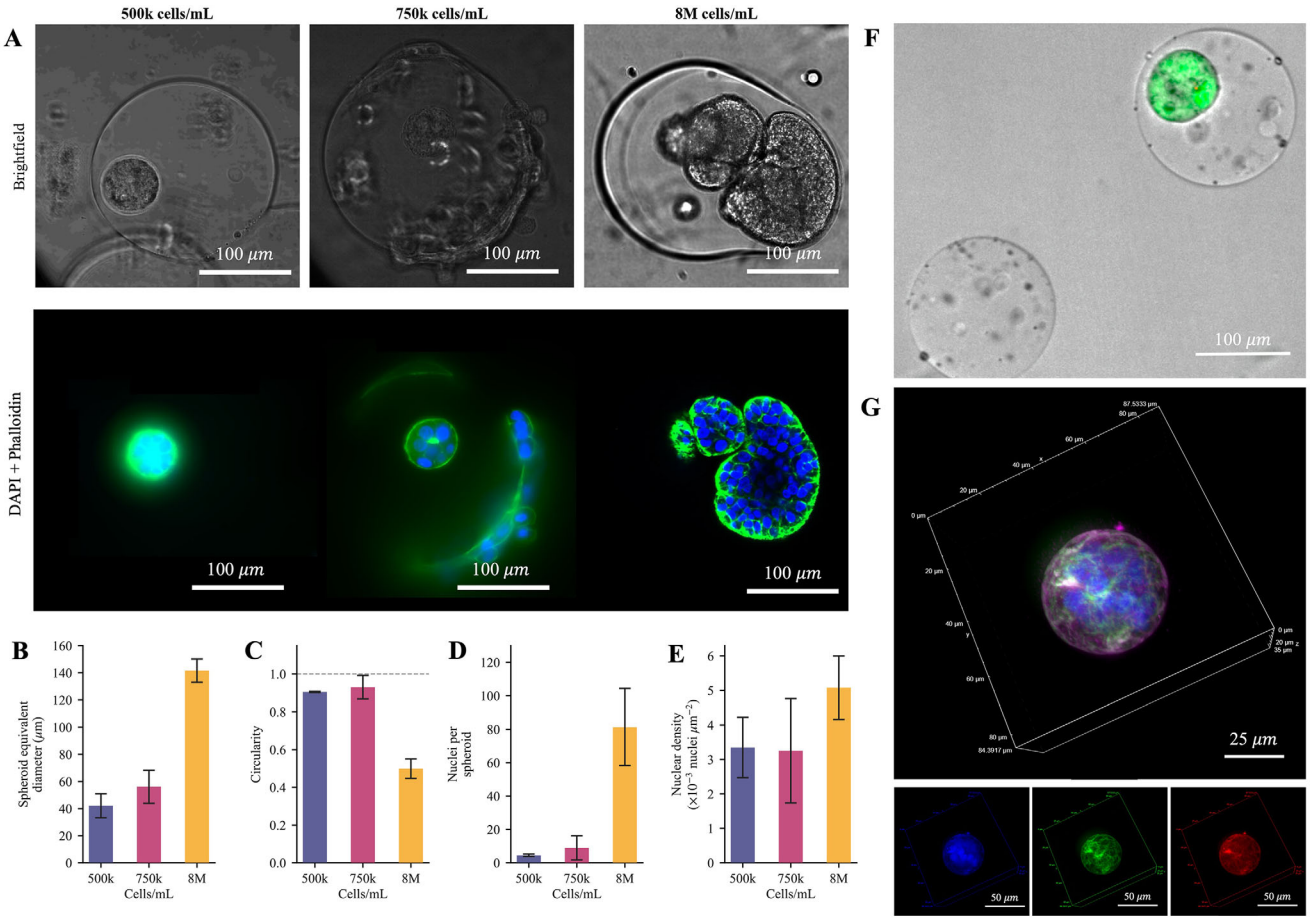

FIGURE 6 | Quantitative and qualitative assessment of cell encapsulation, viability, and spheroid formation within GelMA microgels. (A) Representative brightfield micrographs of GelMA microgels at Day 5 for initial seeding concentrations of 500 k, 750 k, and 8 M cells/mL, showing condition-dependent spheroid morphology and confinement within the hydrogel template. Scale bars: 100 μm. (Fluorescence row) Maximum intensity projections of fixed spheroids stained for F-actin (Phalloidin-FITC, green) and nuclei (DAPI, blue) after 5 days of culture for the three seeding conditions. Scale bars: 100 μm. (B) Spheroid equivalent diameter; (C) circularity; (D) number of nuclei per spheroid; (E) nuclear density ($\times 10^{-3}$ nuclei μm^{-2}). Values are reported in physical units (μm or nuclei μm^{-2}) following per-condition calibration-factor conversion (0.4333 μm/px for 500 k/750 k; 0.5677 μm/px for 8 M; see Section 2.3 and Section 5.11). Bars represent mean ± SD. (F) Representative LIVE/DEAD fluorescence micrograph of encapsulated A549 cells at Day 5 (500 k cells/mL condition); green signal (calcein-AM) indicates live cells, red signal (ethidium homodimer-1) indicates dead cells, confirming high post-encapsulation viability. Scale bar: 100 μm. (G) Three-dimensional confocal reconstruction of a representative 500 k cells/mL spheroid (2048 × 2048 × 35 planes; XY = 0.108 μm/px; Z = 1.0 μm/slice). Left: XY maximum intensity projection (top view). Right: 3D surface rendering (side view). Three fluorescence channels are shown: DAPI (blue, nuclei), Phalloidin-FITC (green, F-actin), and WGA-AF647 (pink, plasma membranes). The reconstruction confirms compact spherical organization, dense nuclear packing, continuous F-actin cortex, and intact plasma membrane architecture throughout the spheroid volume.

green fluorescence (calcein-AM, live cells) with minimal red signal (ethidium homodimer-1, dead cells) was observed across the spheroid population, confirming high post-encapsulation viability and full adaptation to the hydrogel microenvironment over the culture period.

Brightfield imaging at Day 5 revealed condition-dependent spheroid morphologies across all three seeding densities (Figure 6A). At 500 k cells/mL, compact and well-delimited spheroids were observed within individual microgels, with a circular droplet boundary clearly visible. At 750 k cells/mL, spheroids of comparable size were detected alongside evidence of early surface proliferation. At 8M cells/mL, dense multicellular aggregates occupied the full microgel volume, with irregular boundaries indicative of confinement-limited growth.

Fluorescence imaging of fixed samples stained for F-actin (Phalloidin-FITC, green) and nuclei (DAPI, blue) confirmed organized three-dimensional cellular architecture across all conditions (Figure 6, fluorescence row). At 500 k cells/mL, tightly packed DAPI-positive nuclei were distributed uniformly throughout the spheroid volume, surrounded by a continuous F-actin network consistent with preserved cytoskeletal organization and cell–cell contact. At 750 k cells/mL, fluorescence signals revealed denser nuclear packing with partial overlap of the actin cytoskeleton at the spheroid periphery. At 8 M cells/mL, an extensively organized multicellular aggregate was observed with well-defined actin filament architecture and high nuclear density.

Quantitative morphometric analysis was performed on segmented microgels across all three conditions using an automated

Python-based image analysis pipeline (described in Section S4 and Figure S4) (Figure 6B–E). Spheroid equivalent diameter increased progressively with initial seeding density, circularity remained high at 500 k and 750 k cells/mL, confirming spherical geometry and uniform confinement within the hydrogel template, while it decreased markedly at 8 M cells/mL, reflecting irregular morphology associated with overfilling of the microgel volume. Nuclear count per spheroid and nuclear packing density followed consistent density-dependent trends across all conditions. Quantitative morphometric metrics were converted to physical units using instrument-specific calibration factors of 0.4333 μm/px (500 k and 750 k conditions, 10× objective, 2048 × 2048 px downsampled 4× by the analysis pipeline) and 0.5677 μm/px (8M condition, 20× objective, 4096 × 4096 px downsampled 8×; see Section 5.11).

Three-dimensional confocal reconstruction of a representative 500 k cells/mL spheroid (Figure 6G) confirmed the formation of a compact, structurally coherent multicellular aggregate within the GelMA matrix. The z-stack reconstruction (2048 × 2048 × 35 planes; XY = 0.108 μm/px; Z = 1.0 μm/slice) was performed with simultaneous acquisition of three fluorescence channels: DAPI (blue, nuclei), Phalloidin-FITC (green, F-actin), and WGA-AF647 (pink, plasma membranes). The reconstruction revealed a dense nuclear core enclosed within a continuous F-actin cortex, with plasma membrane labeling delineating individual cell boundaries throughout the spheroid volume. No evidence of central necrosis or structural discontinuity was detected, consistent with viable and well-oxygenated spheroids at this seeding density.

Quantitative analysis of spheroid formation efficiency — defined as the fraction of cell-laden microgels containing at least one morphologically defined spheroid — yielded values of 59.5% at 500 k cells/mL, 51.8% at 750 k cells/mL, and 90.8% at 8×10^6 cells/mL, demonstrating reproducible spheroid formation and identifying 500 k cells/mL as the condition providing optimal balance between confinement, structural integrity, and long-term viability.

3 | Discussion

3.1 | Optimization of the Parameters in the Droplet Microfluidic Device

The integrated design of the microfluidic platform enabled precise spatiotemporal control over droplet formation and GelMA crosslinking, ensuring high reproducibility and monodispersity, which are essential prerequisites for reliable 3D cell culture systems. The flow-focusing junction served as the primary droplet-generation element, governing droplet size through hydrodynamic shear. In addition, the upstream spiral microchannel (Figure S1) was incorporated as a passive hydrodynamic conditioning module to reduce concentration gradients and promote more uniform cell distribution across the channel cross-section before photogelation. While spiral-based inertial focusing and Dean-flow approaches can enable deterministic cell ordering under appropriate high-inertial-regime conditions [32, 33], the benefit of curved channel architectures depends critically on the operating Dean number and flow parameters. In recent demonstrations, improved single-cell encapsulation has been achieved by combining spiral focusing with on-chip enrichment modules [33], and deterministic encapsulation of defined cell clusters has been shown using double-spiral architectures operating in inertial-force-assisted conditions [32]. Within the pressure range selected in this work to maximize droplet generation stability and biological performance, the spiral module is therefore discussed as a conditioning element that supports suspension uniformity and spatial distribution, rather than as a deterministic single-file "cell-train" generator.

The quantitative analysis of cell spatial distribution presented in Section 2.1.2 provides experimental evidence that the spiral microchannel substantially improves suspension uniformity prior to droplet formation, with a 2.8–3.7-fold reduction in the CV of the local density signal consistently observed across all spiral loop positions and across approximately 300 independent frames. The progressive improvement from the outlet loop (2.8×) to the inlet loop (3.7×) — corresponding to increasing path length along the spiral — is consistent with a cumulative passive conditioning effect rather than a threshold-dependent hydrodynamic transition. It is important to contextualise this result within the operating regime of the platform. Under the pressure-driven conditions employed ($P_D = 60$ mbar), the estimated mean flow velocity in the spiral channel is approximately 30 mm s^{-1}, yielding a Reynolds number $Re < 5$ and a Dean number $De < 1$ for the spiral geometry (channel width 170 μm, height 100 μm, length 53 mm). These values place the system firmly outside the inertial-focusing regime, in which lateral cell migration toward equilibrium positions across the channel cross-section would require $De \gg 1$ and sufficiently high Re to generate the lift forces responsible for deterministic cell ordering [32, 33]. Accordingly, the spiral is not interpreted here as an inertial focusing or Dean-flow cell aligner, but as a passive hydrodynamic preconditioning element whose beneficial effect on suspension uniformity is attributed to a combination of physically plausible contributing factors.

First, the 53 mm curved path length provides substantially greater transit time than a direct inlet connection, allowing the continuous curvature to counteract gravitational sedimentation — the primary driver of cell clustering at the base of the channel cross-section — by periodically reorienting the effective gravitational direction relative to the channel geometry as cells traverse successive loops. Second, the double-spiral architecture with central flow inversion (Figure S1) imparts directional changes to the flow trajectory that, while individually weak at $De < 1$, may accumulate over the full channel length to produce macroscopic redistribution of cells across the cross-section. Third, the extended hydrodynamic path length increases the number of geometry-driven trajectory perturbations experienced by each cell before reaching the junction, further contributing to the dispersal of transient soft aggregates that form at high seeding densities. While these mechanisms are plausible and consistent with the observed data, we acknowledge that their individual contributions cannot be decoupled from the present experiment and that a direct mechanistic demonstration would require dedicated flow visualisation studies beyond the scope of this work.

It should further be noted that the characterisation of spiral preconditioning was deliberately performed at 8×10^6 cells/mL

to maximise signal detectability, whereas encapsulation experiments were conducted at 500 × 10^3–8 × 10^6 cells/mL. The preconditioning mechanism described above is governed by channel geometry and path length, which are independent of cell concentration; the effect reported here therefore represents a conservative, upper-bound characterisation of distribution heterogeneity, and the qualitative improvement in suspension uniformity is expected to persist — albeit with lower absolute signal contrast — across all encapsulation concentrations.

Finally, it is worth noting that the local intensity variance proxy used to quantify cell distribution in this analysis is an indirect signal that reflects local optical heterogeneity rather than directly counting individual cells. At the operating density of 8 × 10^6 cells/mL, individual cell segmentation is not feasible by brightfield imaging, and the variance signal was validated as a consistent proxy by its physically interpretable spatial patterns — inlet-region clustering in the no-spiral condition, loop-position-dependent uniformity in the spiral condition — and by the temporal stability of the CV across the full acquisition window (Figure 3C). Representative QC overlays showing channel masks and local variance signal maps for both conditions are provided in Figure S3. These properties collectively support the use of this metric as a robust, semi-quantitative descriptor of suspension homogeneity in the present experimental context.

The subsequent purification workflow (Figure 1B) further confirmed the compatibility of the overall process with biological materials, preserving the structural integrity and morphology of the GelMA microgels after synthesis. Altogether, the optimized device geometry and downstream handling established the physical and operational foundation for the following analyses of droplet formation, swelling dynamics, and biological validation.

The results of Section 2.2.1 demonstrate that droplet formation at the flow-focusing junction follows a shear-driven breakup mechanism characteristic of confined microfluidic geometries. Increasing the continuous-phase pressure (P_C) enhanced local shear, accelerating the detachment of the dispersed GelMA thread and producing smaller droplets, consistent with the viscous–capillary scaling law ($f \propto Ca$, with $Ca = \mu_c U_c/\gamma$). The progressive reduction of ECD with pressure increase confirmed that viscous forces dominate over interfacial tension, and that at higher flow rates the regime approaches a dripping-to-jetting transition, where droplet size becomes less sensitive to further pressure increments.

Among the tested conditions, the 60/70 mbar configuration provided the optimal balance between generation stability and droplet volume, maintaining a uniform dripping regime and producing droplets large enough to support cell viability and diffusion in 3D culture. This operating point was therefore selected not only for hydrodynamic reproducibility but also for biological functionality, since droplets of larger volume offer enhanced nutrient transport and reduce confinement stress during cellular proliferation (Section 3.2). These hydrodynamic optimizations define the baseline conditions for analyzing the swelling and microstructural behavior of the resulting GelMA microgels (Section 2.2.2–2.2.4).

The swelling profiles reported in Section 2.2.2 and illustrated in Figure 4E,F reveal that GelMA microgels exhibit solvent- and temperature-dependent hydration dynamics regulated by osmotic and ionic interactions.

At 21°C, the nearly constant diameter in distilled water (≈ 310 μm over 48 h) corresponds to a quasi-equilibrium state governed by hydrogen bonding between water molecules and gelatin chains in the absence of ionic screening. This stabilization minimizes volumetric fluctuations and reflects the strong hydrophilic affinity of the network [34–36].

In contrast, in PBS and RPMI media, the initial shrinkage observed within 3–6 h corresponds to transient deswelling induced by ionic screening of negatively charged carboxyl groups on the GelMA backbone.

As counterions (Na^+, Cl^-, Ca^{2+}) diffuse into the matrix, they neutralize internal charges, lower osmotic pressure, and induce temporary chain contraction. Subsequently, as ionic bridges and hydrogen-bond rearrangements form, the gels gradually reswell to a new equilibrium state (ECD ≈ 130 μm), typical of weakly polyelectrolytic hydrogels where charge screening and elasticity coexist [34, 35].

At 37°C, the modest increase in final diameter (PBS ≈ 145 μm; RPMI ≈ 138 μm) indicates that GelMA retains elastic recovery and hydration capacity at physiological temperature. The biphasic behavior observed in distilled water at 37°C, characterized by an initial contraction followed by progressive reswelling, may be associated with temperature-induced relaxation and rearrangement of the GelMA polymer network immediately after rehydration. The transient decrease in diameter could reflect local chain reorganization and partial network contraction, whereas longer incubation promotes water uptake and equilibration of the crosslinked matrix. This behavior may also be influenced by the thermoresponsive nature of gelatin-derived materials, including conformational transitions of gelatin chains that have been reported near the gelatin sol–gel transition temperature [33, 34]. However, the present experiments were not specifically designed to isolate this mechanism, and additional studies would be required to establish a direct relationship between the observed swelling response and LCST-like behavior. Such reversible hydration provides a favorable balance between mechanical integrity and dynamic water uptake, allowing GelMA microgels to adapt to environmental changes while preserving scaffold structure—an essential property for 3D culture and drug delivery applications (Section 3.2).

The rheological characterisation (Figure 4G–I) presented in Section 2.2.3 clarifies the role of the MC additive within the formulation. At the 0.1% w/v concentration employed, well below the entanglement threshold of methylcellulose [37], MC acts as a minor rheological modifier rather than as a viscoelastic focusing agent. Its principal measurable effect is an increase in low-shear viscosity by approximately one order of magnitude (Figure 4G), expected to mitigate gravitational sedimentation of cells under the quasi-static conditions prevailing in the reservoir, tubing, and during flow interruptions. Notably, at the high shear rates

characteristic of flow within the spiral channel ($\dot{\gamma}$ of order 10^2–10^3 s^{-1} at the operating velocity of ≈30 mm s^{-1}), the two viscosities are already converging at the upper end of the measured range, indicating that MC and the spiral preconditioning module act in complementary shear regimes: the former contributes to suspension stability under low-shear/quiescent conditions, while the latter governs cell redistribution during active high-shear transit. Photorheology further demonstrated that MC does not alter the photocrosslinking kinetics of GelMA (Figure 4H), confirming that its inclusion improves handling of the cell suspension without compromising the in situ gelation step central to the platform.

The SEM characterization presented in Section 2.2.4 provides morphological evidence of the structural organization generated by the combined effects of droplet microfluidic fabrication, photocrosslinking, and freeze-drying. In contrast to the smooth and spherical hydrated microgels observed immediately after production and purification (Section 2.2.1, Figure 4A,B), lyophilized particles exhibited pronounced structural collapse and a highly porous sponge-like morphology (Figure 5).

This transition reflects the intrinsic water-rich nature of the GelMA hydrogel network previously highlighted by the swelling experiments discussed in Section 2.2.2. During rapid freezing in liquid nitrogen, water confined within the crosslinked hydrogel forms ice domains throughout the particle volume. Subsequent lyophilization removes these frozen solvent regions through sublimation, generating the interconnected porous architecture observed in Figure 5D.

Importantly, despite the extensive morphological rearrangement induced by dehydration, the microgels maintained their overall structural integrity without evidence of fragmentation or catastrophic collapse. This observation indirectly confirms the effectiveness of the UV-induced crosslinking process described in Section 2.1, suggesting the formation of a mechanically stable GelMA network capable of withstanding substantial solvent removal.

The porous architecture observed after freeze-drying may additionally contribute to enhanced diffusion and mass transport upon rehydration, properties particularly relevant for the biological applications discussed in Section 2.3, where nutrient exchange and long-term cellular viability within the hydrogel microgels are critical parameters for spheroid formation and maintenance.

3.2 | Cellular Encapsulation and Biological Validation

The biological validation presented in Section 2.3 demonstrates that the Spheroid-on-a-Drop platform enables cytocompatible cell encapsulation and supports progressive three-dimensional spheroid formation within GelMA microgels over five days of culture. The LIVE/DEAD imaging at 500k cells/mL (Figure 6F) confirms that high viability is maintained across the spheroid population at the lower seeding density, collectively validating the biocompatibility of both the microfluidic processing and the in situ UV crosslinking step across the full range of tested conditions.

The morphometric analysis (Figure 6B–E) reveals a clear seeding-density-dependent transition in spheroid phenotype. At 500 k cells/mL, high circularity values and moderate nuclear counts confirm the formation of compact, geometrically well-defined spheroids confined within the microgel template — the ideal outcome for controlled 3D tumor modeling. At 750 k cells/mL, the slight reduction in circularity and increased surface proliferation signal an early transition toward confinement stress, while at 8 M cells/mL the pronounced drop in circularity and irregular aggregate morphology indicate that the hydrogel volume is insufficient to support ordered spheroid assembly at this density. These observations are consistent with diffusion-limited oxygen and nutrient transport at high cell densities, a well-established constraint in scaffold-based 3D culture systems.

The three-dimensional reconstruction of a 500k cells/mL spheroid (Figure 6G) provides direct structural evidence of organized multicellular assembly within the GelMA matrix. The simultaneous visualization of nuclei (DAPI), F-actin cytoskeleton (Phalloidin), and plasma membranes (WGA-AF647) confirms tight intercellular contacts, preserved cytoskeletal architecture, and continuous membrane organization throughout the spheroid volume — hallmarks of viable epithelial tumor spheroids with maintained polarity. The absence of a necrotic core at this seeding density further supports the suitability of the 500 k cells/mL condition for downstream functional assays requiring uniform viability. The spheroid formation efficiency observed at 500 k cells/mL (59.5%) reflects the stochastic nature of Poisson-limited cell loading under the present operating conditions, where a fraction of microgels receives insufficient cells to initiate compact aggregate formation. This value can be modulated by adjusting the initial cell concentration, as demonstrated by the spheroid-forming fractions observed across the tested seeding densities (59.5%, 51.8%, and 90.8% at 500 k, 750 k, and 8×10^6 cells/mL, respectively). Further improvements may be achieved by optimizing the pressure ratio to increase droplet volume — thereby accommodating more cells per microgel at a given suspension density — or by implementing active co-encapsulation strategies such as deterministic pairing modules or pre-clustering approaches. However, the 500k cells/mL condition was deliberately selected as the biologically optimal working point, as the higher spheroid formation efficiency at 8M cells/mL comes at the cost of reduced circularity and evidence of confinement-limited growth, which compromise spheroid structural integrity and downstream functional utility.

Collectively, these results validate Spheroid-on-a-Drop as a reproducible platform for the generation of cytocompatible, structurally defined GelMA-based 3D tumor spheroids. The combination of rheological tuning, hydrodynamic preconditioning, and biomimetic hydrogel chemistry provides a scalable single-material system suitable for applications in tumor modeling, drug screening, and mechanobiological investigations.

4 | Conclusion and Future Outlook

In this work, we presented an integrated droplet-based microfluidic platform for the generation of GelMA microgels optimized for 3D cell encapsulation and spheroid culture. Through sys-

tematic optimization of operating parameters, we established a clear correlation between flow conditions, droplet formation dynamics, and resulting microgel morphology. The flow-focusing design ensured stable and reproducible droplet production, while the inclusion of an upstream spiral channel provided hydrodynamic conditioning that supported suspension uniformity prior to gelation. The produced GelMA microgels exhibited high monodispersity, structural integrity, and tunable swelling behavior across different osmotic and thermal conditions. SEM analysis revealed a homogeneous internal morphology after lyophilization, consistent with uniform crosslinking and high water content, supporting predictable rehydration and mass transport upon reswelling. The biological validation using A549 human lung carcinoma cells demonstrated that the microfluidic encapsulation process preserves cell viability and supports long-term 3D culture. Encapsulated cells organized into compact and viable spheroids within the GelMA matrix, confirming both the cytocompatibility of the process and the functional suitability of the microgels as microcarriers.

Overall, the proposed Spheroid-on-a-Drop platform represents a reproducible and scalable approach for the fabrication of biocompatible GelMA-based microgels. Its precise control over droplet dynamics and cell distribution paves the way for advanced applications in tissue modeling, drug screening, and personalized medicine, providing a solid foundation for future biofabrication strategies integrating microfluidics and biomaterials.

The next phase of this research will focus on extending the *Spheroid-on-a-Drop* model to different cell types, including patient-derived organoids from metastatic colorectal cancer, to assess its adaptability across diverse biological systems. Parallel efforts will aim at developing next-generation microfluidic devices capable of active hydrodynamic manipulation of droplets, enabling controlled fusion, nutrient exchange, and long-term on-chip organoid growth. This evolution will move the platform beyond static encapsulation toward dynamic organoid-on-chip systems, bridging the gap between in vitro modeling and physiologically relevant tumor microenvironments.

5 | Material and Methods

5.1 | Chemical Reagents

Gelatin type A (from porcine skin), methacrylic anhydride (MA), and methylcellulose (MC, 400 cP) were purchased from Sigma-Aldrich (St. Louis, MO, USA). Mineral oil (M8410) and sorbitan monooleate (Span 80, Sigma-Aldrich) were used as the oil phase and surfactant, respectively. Lithium phenyl-2,4,6-trimethylbenzoylphosphinate (LAP) was obtained from TCI Chemicals (Shanghai, China) and used as a photoinitiator. All reagents were used as received without further purification.

5.2 | Microfluidic Chip Fabrication

The microfluidic devices were fabricated using standard photolithographic and soft lithography techniques. Briefly, the device design was drafted using Rhinoceros 3D (version 8, Robert McNeel & Associates, USA) and transferred onto a chrome-on-quartz photomask produced via a high-resolution laser writer (LW405, Microtech Srl, Italy). A 4″ silicon wafer was spin-coated with SU-8 2050 negative photoresist (Kayaku Advanced Materials, USA) to obtain a target feature height of 100 μm, following the manufacturer's protocol for photolithography. After UV exposure through the photomask and subsequent post-exposure bake, the wafer was developed in SU-8 developer (MicroChem, USA) to generate the master mold. To facilitate PDMS demolding, the SU-8 masters were silanized overnight in a desiccator saturated with trimethylchlorosilane (TMCS, Sigma-Aldrich, USA).

PDMS replicas were fabricated by casting poly(dimethylsiloxane) (Sylgard 184, Dow Corning) at a 10:1 (w/w) base-to-curing agent ratio onto the silanized master, followed by thermal curing at 70°C for 2 h. After curing, the PDMS slabs were peeled off, and inlet/outlet holes were created using a 1.5 mm biopsy puncher. Devices were irreversibly bonded onto 1″ × 3″ microscope glass slides by oxygen plasma treatment (Femto Plasma Etcher, Diener electronic, Ebhausen, Germany).

To improve channel hydrophobicity, the microfluidic channels were silanized by flowing nitrogen gas saturated with TMCS vapor for 15 min, followed by thermal treatment at 140°C for 10 min.

5.3 | GelMA Synthesis

Gelatin methacryloyl (GelMA) with a degree of functionalization of 95% (GelMA A95) was synthesized from type A gelatin (porcine skin, Sigma Aldrich) following previously reported protocols [36, 38, 39]. The lyophilized product was stored at room temperature in the dark, until use.

5.4 | Microgels Generation

To generate GelMA-based microgels, two separate solutions were injected into the microfluidic device: for the dispersed phase, a solution of GelMA (7.5% w/v) supplemented with methylcellulose (MC, 0.1% w/v) and the photoinitiator lithium phenyl-2,4,6-trimethylbenzoylphosphinate (LAP, 2.5 mg/mL) was prepared in empty RPMI medium and used, while the continuous phase consisted of mineral oil (Sigma Aldrich, M8410) containing 3% (v/v) Span 80 (Sigma Aldrich).

Droplet formation was achieved in a flow-focusing geometry by applying pressures of 60 mbar for the dispersed phase and 70 mbar for the continuous phase. Crosslinking of GelMA droplets into microgels was induced by exposure to a dual-channel Prizmatix FC5 multi-wavelength LED system (Prizmatix Ltd., Israel), equipped with two fiber-coupled 405 nm light sources operating at 5.5% and 9.0% of full power (corresponding to ≈ 60 mW cm^{-2} and 100 mW cm^{-2}, respectively). The irradiation was applied perpendicularly to the outlet channel for 5 s to ensure complete photopolymerization. Crosslinking was therefore performed on-chip immediately after droplet formation and before collection, minimizing sedimentation-driven cell redistribution and promoting uniform network formation throughout the hydrogel volume.

After generation, the microgels were rinsed three times with RPMI culture medium and centrifuged at 190 g for 5 min (TG16-W centrifuge, Cence) to remove residual mineral oil. Unless otherwise stated, the GelMA concentration was fixed at 7.5% (w/v). For cell encapsulation experiments, all steps were performed under sterile conditions.

For morphological analysis, freshly prepared GelMA microgels were first washed one time with phosphate-buffered saline (PBS, pH 7.4) and then two times with distilled water to remove residual oil and surfactant. The samples were then transferred into sterile microtubes, rapidly frozen by direct immersion in liquid nitrogen, and subsequently lyophilized using a bench-top freeze dryer (FreeZone 2.5, Labconco, USA) operating under a chamber pressure of 0.01 mbar for 24 h. This procedure ensured complete sublimation of ice crystals, preserving the internal microstructure of the hydrogel network. The resulting dry microgels were stored in a desiccator until further morphological characterization by scanning electron microscopy (SEM) (Section 5.6).

5.5 | Microgels Characterization

The size of GelMA microgels obtained under different flow pressure configurations was measured by optical microscopy (Leica, Germany) and quantified using ImageJ software (NIH, USA). Droplet generation frequency was evaluated using an Eclipse Ti2 Nikon microscope equipped with a Crest X-Light spinning disk through time-lapse acquisition. Swelling behavior was monitored by optical microscopy at defined time points (T0: 0 h; T1: 3 h; T2: 6 h; T3: 24 h; T4: 48 h) in distilled water, PBS, and complete RPMI culture medium at 21°C and 37°C, and analyzed using ImageJ.

5.6 | Rheological Characterisation

The rheological behaviour of the GelMA-based formulations was characterised using a modular compact rheometer (Physica MCR 302, Anton Paar) in parallel-plate geometry (25 mm diameter). Steady-shear flow measurements were performed on the uncured (liquid) formulations at 25°C with a plate gap of 300 µm, sweeping the shear rate from 0.1 to 100 s^{-1}, to determine the rotational viscosity of GelMA A95 7.5% w/v and GelMA A95 7.5% w/v + MC 0.1% w/v.

Real-time photorheology was performed on the same instrument, equipped with a 405 nm LED light source (2-channel LED, Prizmatix; 17 mW cm^{-2}) positioned beneath the lower glass plate, at 25°C and 37°C with a plate gap of 300 µm, at a constant angular frequency of 10 rad s^{-1} and a strain amplitude of 5% (within the linear viscoelastic region determined by preliminary amplitude sweep). The storage (G′) and loss (G″) moduli were monitored during irradiation; to allow signal stabilisation, the light was switched on after a 30 s equilibration period.

Amplitude sweeps were performed on the crosslinked hydrogels at 25°C and 37°C, sweeping the strain amplitude from 0.1% to 1000% at a constant angular frequency of 10 rad s^{-1}, to assess the linear viscoelastic region; samples were crosslinked in situ on the rheometer plate prior to the sweep. All measurements were performed in triplicate

5.7 | SEM Characterization

GelMA microgels generated according to the protocol described in Section 5.4 (“Microgels Generation”) were morphologically characterized by scanning electron microscopy (SEM) following freeze-drying. After purification and washing, the microgels were rapidly frozen by direct immersion in liquid nitrogen and subsequently lyophilized overnight to remove residual water prior to imaging.

The dried samples were mounted onto conductive aluminum stubs using carbon adhesive tabs and sputter-coated with a 200 nm platinum layer to minimize charging effects during electron beam exposure and improve signal stability during imaging. SEM imaging was performed using a TESCAN CLARA field-emission scanning electron microscope (FEG-SEM) operated under high-vacuum conditions at low accelerating voltage to preserve the delicate morphology of the freeze-dried hydrogel structures. Images were acquired at multiple magnifications to evaluate both the overall morphology and the internal porous microarchitecture of the lyophilized microgels.

The observed porous morphology results from ice crystal formation during cryogenic freezing and subsequent sublimation during lyophilization, which generates voids within the photocrosslinked GelMA network. Morphological analysis was qualitatively correlated with the swelling behavior described in Section 2.2.2 and with the photocrosslinking conditions reported in Section 2.1.

5.8 | Brightfield Videomicroscopy and Quantitative Analysis of Cell Spatial Distribution

To evaluate the effect of the spiral microchannel on cell spatial distribution prior to droplet encapsulation, a dedicated brightfield videomicroscopy experiment was performed under two flow configurations: a spiral preconditioning condition, in which the dispersed phase traversed the full spiral channel before reaching the flow-focusing junction, and a no-spiral reference condition, in which the dispersed phase was directed to the junction without spiral preconditioning. Both configurations were operated at an inlet pressure of 60 mbar, using a dispersed phase composed of GelMA (7.5% w/v) supplemented with MC (0.1% w/v) and A549 cells at a seeding density of 8×10^6 cells/mL in complete RPMI 1640 medium, maintained at 37°C throughout acquisition. This characterisation experiment was performed exclusively at 8×10^6 cells/mL, as this elevated density amplifies spatial heterogeneity to levels reliably detectable by brightfield intensity analysis at 5× magnification; at the concentrations employed for encapsulation (500×10^3, 750×10^3, and 8×10^6 cells/mL; see Section 5.9), local concentration gradients are insufficient to produce robust signal differences under the imaging conditions described below. The hydrodynamic regime of the characterisation experiment is otherwise identical to that of the encapsulation experiments, as flow conditions and dispersed-phase rheology are governed by the GelMA–MC matrix rather than by cell concentration.

Videos were acquired at 5× magnification using an Eclipse Ti2 Nikon microscope equipped with a Crest X-Light spinning disk at 5.0 fps, yielding 1920 × 1080 pixel frames. For the no-spiral condition, imaging was performed at the channel inlet region upstream of the flow-focusing junction. For the spiral condition, imaging was performed across three loop positions: outlet loop (outermost), intermediate loop, and inlet loop (innermost). Frames were extracted at a fixed interval of 5 frames from the full acquisition to reduce inter-frame temporal redundancy.

Cell spatial distribution was quantified frame-by-frame through a local intensity variance signal computed within a 21 × 21 pixel sliding window, applied within a binary channel mask defined independently for each configuration from the visible wall boundaries of the brightfield image. The coefficient of variation (CV) of the in-mask signal was used as a dimensionless index of spatial heterogeneity for each frame. The full description of mask definition, signal computation, polarity convention, normalisation, and axial profile analysis is provided in Section S3. Statistical comparison of per-frame CV distributions between the no-spiral condition and each spiral loop was performed using a two-sided Mann–Whitney U test (N = 310 frames, no-spiral; N = 204–244 frames per loop, spiral), consistent with the non-parametric framework described in Section 5.12.

5.9 | Cell Culture

Human lung cancer cell line, A549, were kindly provided by Dr. Valentina Monica, Department of Oncology, University of Torino, AOU San Luigi Gonzaga. Cells were cultured in Gibco BenchStable RPMI 1640 GlutaMAXTM medium (Thermo Fisher) supplemented with 10% Fetal Bovine Serum (Sigma Aldrich) and 1% penicillin/streptomycin (Sigma Aldrich) in a humidified incubator at 37°C, 5% CO_2.

To perform cell encapsulation, A549 were harvested from culture flasks using a standard detachment protocol. Briefly, the culture medium was aspirated, and the cell monolayer was washed once with Dulbecco's Phosphate-Buffered Saline solution (DPBS, Sigma-Aldrich), trypsinized (Trypsin, Sigma-Aldrich) and centrifuged at 190 g for 5 min. Cells were resuspended in GelMA (7.5% w/v in Gibco BenchStable RPMI 1640 GlutaMAX medium) at final concentrations of 500 000, 750 000, and 8×10^6 cell/mL. The obtained solutions were used for GelMA microgels formation, as previously reported in Section 5.4.

After generation, the microgels with embedded cells were washed three times with complete RPMI medium and centrifuged at 190 g for 5 min to remove residual mineral oil. After the last washing step, microgels were resuspended in 10 mL of fresh complete RPMI and 50 µL and seeded into 48 well plate; 100 µL of fresh culturing medium was added in each well at seeding time and after 4 days. Cells were maintained in culture within GelMA microgels for 5 days.

5.10 | Fluorescence Microscopy

LIVE/DEAD Assay: Cell viability at Day 5 for the 500k cells/mL condition was assessed using the LIVE/DEAD Cell Viability Kit (Sigma-Aldrich). Each sample well was stained by adding 100 µL of DPBS solution containing kit solution B (1:1000, ethidium homodimer-1) and kit solution A (1:500, calcein-AM), followed by incubation for 30 min at 37°C. Fluorescence signals were detected using Eclipse Ti2 Nikon microscope equipped with a Crest X-Light spinning disk unit.

Immunofluorescence Staining for Spheroid Characterization: Samples were collected after 5 days of culture and centrifuged at 190 × g for 5 min. Pellets were resuspended in DPBS, washed, and fixed in 4% paraformaldehyde (PFA, Alfa Aesar) for 1 h at room temperature, followed by three washes with DPBS, and stored at 4°C. Samples were then stained with WGA Alexa Fluor 647 conjugate (10 µg/mL, Thermo Fisher Scientific) for 1 h at room temperature to label plasma membranes (pink channel). After one wash with DPBS (400 × g, 5 min), cells were permeabilized with 0.25% Triton X-100 (Sigma-Aldrich) in DPBS for 30 min at room temperature, followed by one wash. Samples were then incubated for 4 h at room temperature in staining solution containing DAPI (0.4 mM, Sigma-Aldrich) for nuclear visualization (blue channel) and Phalloidin-FITC (1 mg/mL, Sigma-Aldrich) for F-actin labeling (green channel). After a final wash (400 × g, 5 min), samples were resuspended in DPBS for imaging.

2D Fluorescence Imaging: Wide-field fluorescence images were acquired on an Eclipse Ti2 Nikon microscope equipped with a Crest X-Light spinning disk unit. Maximum intensity projections were generated in ImageJ (NIH, USA).

3D Confocal z-Stack Acquisition: Three-dimensional imaging of representative 500k cells/mL spheroids was performed on the same Eclipse Ti2 Nikon system. Z-stacks were acquired over 35 optical planes (total depth ≈ 35 µm; XY pixel size: 0.108 µm/px; Z step: 1.0 µm/slice) with simultaneous acquisition of three fluorescence channels: CH0 = DAPI (blue, nuclei), CH1 = Phalloidin-FITC (green, F-actin), CH2 = WGA-AF647 (pink, plasma membranes). Maximum intensity projections and the 3D surface rendering shown in Figure 6G were generated directly from the confocal acquisition software.

5.11 | Automated Morphometric Analysis of Spheroids

Quantitative morphometric characterization of GelMA-encapsulated spheroids was performed using a custom Python-based image analysis pipeline. Brightfield and fluorescence TIFF images were loaded using the tifffile library. Spheroid boundaries were identified using the Cellpose cyto3 deep-learning model applied to a combined input channel computed as the pixel-wise maximum of the normalized F-actin and DAPI images (MAX(Ph, DAPI)), followed by morphological refinement, as detailed in Section S4. Cell nuclei were segmented from the DAPI channel using the Cellpose nuclei model, with subsequent filtering by area and circularity thresholds to exclude debris and incompletely segmented objects. Surface-growth morphologies were excluded by manual quality control based on brightfield morphology.

For each segmented spheroid the following metrics were extracted: equivalent circular diameter (ECD, px), circularity ($4\pi \cdot$ area / perimeter^2), number of DAPI-positive nuclei per spheroid, and nuclear density (nuclei μm^{-2}). Physical calibration was applied per condition using instrument-specific factors: 0.4333 µm/px for the 500 k and 750 k conditions (10× objective; 2048 × 2048 px, 4× pipeline downsampling) and 0.5677 µm/px for the 8M condition (20× objective; 4096 × 4096 px, 8× pipeline downsampling). Nuclear density is reported in nuclei μm^{-2}.

Statistical comparisons across conditions were performed using one-way ANOVA with Tukey post-hoc correction for normally distributed variables, or Kruskal–Wallis with Dunn correction where normality was rejected by Shapiro–Wilk test ($\alpha = 0.05$). All analyses were implemented in Python using scipy.stats, pandas, and matplotlib. Analysis scripts are available from the corresponding author upon reasonable request.

5.12 | Statistics

All experiments were performed in triplicate unless otherwise specified. For microgel size and generation frequency measurements, the properties of 30 individual droplets were quantified per condition across three independent replicates. Data are presented as mean ± standard deviation (SD).

For droplet generation frequency, a one-way ANOVA with Tukey's multiple comparison post-test was applied. For equivalent circular diameter analysis, data were assessed using a Brown–Forsythe and Welch one-way ANOVA followed by Dunnett's T3 multiple comparison test to account for unequal variances. For cell spatial distribution analysis, per-frame CV distributions were compared between the no-spiral condition and each spiral loop using a two-sided Mann–Whitney U test (see Section 5.8; Section S3). Before applying one-way ANOVA, data normality was assessed using the Shapiro–Wilk test and homogeneity of variances was evaluated using Levene's test. ANOVA was performed only when both assumptions were satisfied. When these assumptions were not met, non-parametric statistical tests were employed as appropriate.

A significance threshold of $p < 0.05$ was considered statistically significant throughout. All analyses were performed using GraphPad Prism (version 9.0, GraphPad Software, USA) or Python (*scipy.stats*, version ≥ 1.10).

Author Contributions

A. Cosola: investigation, validation, formal analysis, data curation. **A. Fergola**: investigation, writing – original draft, writing – review and editing, visualization, validation, methodology, formal analysis, data curation, conceptualization. **C. F. Pirri**: project administration, supervision, resources, funding acquisition. **S. L. Marasso**: supervision. **F. Frascella**: writing – review and editing, conceptualization, supervision, project administration, funding acquisition. **M. Cocuzza**: supervision. **L. Napione**: supervision. **V. Vighetto**: conceptualization, investigation, writing – original draft, writing – review and editing, methodology, supervision, data curation. **G. Mesiano**: investigation, writing – review and editing, supervision.

Acknowledgements

Project PNC 0000001 D3 4 Health, the National Plan for Complementary Investments to the NRRP, funded by the European Union—NextGenerationEU.

Open access publishing facilitated by Politecnico di Torino, as part of the Wiley - CRUI-CARE agreement.

Conflicts of Interest

The authors declare no conflicts of interest.

Data Availability Statement

The data that support the findings of this study are available from the corresponding author upon reasonable request.

References

1. Y. Ai, R. Xie, J. Xiong, and Q. Liang, "Microfluidics for Biosynthesizing: From Droplets and Vesicles to Artificial Cells," *Small* 16 (2020): 1903940, https://doi.org/10.1002/smll.201903940.

2. Y. Ding, P. D. Howes, and A. J. deMello, "Recent Advances in Droplet Microfluidics," *Analytical Chemistry* 92 (2020): 132–149, https://doi.org/10.1021/acs.analchem.9b05047.

3. D. Zhang, W. Liu, L. Feng, et al., "Innovative Advances in Droplet Microfluidics," *Research* 8 (2025): 0856, https://doi.org/10.34133/research.0856.

4. C. Liu and X. Xu, "Droplet Microfluidics for Advanced Single-Cell Analysis," *Smart Medicine* 4 (2025): 70002, https://doi.org/10.1002/smmd.70002.

5. S. C. Lesher-Pérez, G.-A. Kim, C. Kuo, et al., "Dispersible Oxygen Microsensors Map Oxygen Gradients in Three-Dimensional Cell Cultures," *Biomaterials Science* 5 (2017): 2106–2113, https://doi.org/10.1039/C7BM00119C.

6. P. Xia, K. Zhang, Y. Gong, G. Li, S. Yan, and J. Yin, "Injectable Stem Cell Laden Open Porous Microgels That Favor Adipogenesis: In Vitro and in Vivo Evaluation," *ACS Applied Materials & Interfaces* 9 (2017): 34751–34761, https://doi.org/10.1021/acsami.7b13065.

7. A. Faulkner-Jones, S. Greenhough, J. A. King, J. Gardner, A. Courtney, and W. Shu, "Development of a Valve-Based Cell Printer for the Formation of Human Embryonic Stem Cell Spheroid Aggregates," *Biofabrication* 5 (2013): 015013, https://doi.org/10.1088/1758-5082/5/1/015013.

8. H. Huang, Y. Yu, Y. Hu, X. He, O. Berk Usta, and M. L. Yarmush, "Generation and Manipulation of Hydrogel Microcapsules by Droplet-Based Microfluidics for Mammalian Cell Culture," *Lab on A Chip* 17 (2017): 1913–1932, https://doi.org/10.1039/C7LC00262A.

9. H. Nazari, A. Heirani-Tabasi, S. Ghorbani, et al., "Microfluidic-Based Droplets for Advanced Regenerative Medicine: Current Challenges and Future Trends," *Biosensors (Basel)* 12 (2021): 20, https://doi.org/10.3390/bios12010020.

10. E. Tumarkin and E. Kumacheva, "Microfluidic Generation of Microgels From Synthetic and Natural Polymers," *Chemical Society Reviews* 38 (2009): 2161, https://doi.org/10.1039/b809915b.

11. L. Amirifar, M. Besanjideh, R. Nasiri, et al., "Droplet-Based Microfluidics in Biomedical Applications," *Biofabrication* 14 (2022): 022001, https://doi.org/10.1088/1758-5090/ac39a9.

12. X. Xu, S. Cheung, X. Jia, et al., "Trends in Organ-on-a-Chip for Pharmacological Analysis," *TrAC Trends in Analytical Chemistry* 180 (2024): 117905, https://doi.org/10.1016/j.trac.2024.117905.

13. N. Shembekar, C. Chaipan, R. Utharala, and C. A. Merten, "Droplet-Based Microfluidics in Drug Discovery, Transcriptomics and High-Throughput Molecular Genetics," *Lab on A Chip* 16 (2016): 1314–1331, https://doi.org/10.1039/C6LC00249H.

14. Y. Ai, F. Zhang, C. Wang, R. Xie, and Q. Liang, "Recent Progress in Lab-On-A-Chip for Pharmaceutical Analysis and Pharmacological/Toxicological Test," *TrAC Trends in Analytical Chemistry* 117 (2019): 215–230, https://doi.org/10.1016/j.trac.2019.06.026.

15. R. Salomon, D. Kaczorowski, F. Valdes-Mora, et al., "Droplet-Based Single Cell RNAseq Tools: A Practical Guide," *Lab on A Chip* 19 (2019): 1706–1727, https://doi.org/10.1039/C8LC01239C.

16. D. J. Collins, A. Neild, A. deMello, A.-Q. Liu, and Y. Ai, "The Poisson Distribution and Beyond: Methods for Microfluidic Droplet Production and Single Cell Encapsulation," *Lab on A Chip* 15 (2015): 3439–3459, https://doi.org/10.1039/C5LC00614G.

17. Y. Cheng, Y. Yu, F. Fu, et al., "Controlled Fabrication of Bioactive Microfibers for Creating Tissue Constructs Using Microfluidic Techniques," *ACS Applied Materials & Interfaces* 8 (2016): 1080–1086, https://doi.org/10.1021/acsami.5b11445.

18. Y. Chen, R. Lin, H. Qi, et al., "Functional Human Vascular Network Generated in Photocrosslinkable Gelatin Methacrylate Hydrogels," *Advanced Functional Materials* 22 (2012): 2027–2039, https://doi.org/10.1002/adfm.201101662.

19. L. E. Bertassoni, M. Cecconi, V. Manoharan, et al., "Hydrogel Bioprinted Microchannel Networks for Vascularization of Tissue Engineering Constructs," *Lab on A Chip* 14 (2014): 2202–2211, https://doi.org/10.1039/C4LC00030G.

20. F. Fu, L. Shang, F. Zheng, et al., "Cells Cultured on Core–Shell Photonic Crystal Barcodes for Drug Screening," *ACS Applied Materials & Interfaces* 8 (2016): 13840–13848, https://doi.org/10.1021/acsami.6b04966.

21. C. Puckert, E. Tomaskovic-Crook, S. Gambhir, G. G. Wallace, J. M. Crook, and M. J. Higgins, "Electro-Mechano Responsive Properties of Gelatin Methacrylate (GelMA) Hydrogel on Conducting Polymer Electrodes Quantified Using Atomic Force Microscopy," *Soft Matter* 13 (2017): 4761–4772, https://doi.org/10.1039/C7SM00335H.

22. K. Yue, G. Trujillo-de Santiago, M. M. Alvarez, A. Tamayol, N. Annabi, and A. Khademhosseini, "Synthesis, Properties, and Biomedical Applications of Gelatin Methacryloyl (GelMA) Hydrogels," *Biomaterials* 73 (2015): 254–271, https://doi.org/10.1016/j.biomaterials.2015.08.045.

23. J. W. Nichol, S. T. Koshy, H. Bae, C. M. Hwang, S. Yamanlar, and A. Khademhosseini, "Cell-Laden Microengineered Gelatin Methacrylate Hydrogels," *Biomaterials* 31 (2010): 5536–5544, https://doi.org/10.1016/j.biomaterials.2010.03.064.

24. B. Parker, R. Samanipour, A. Ahmadi, and K. Kim, "Rapid Fabrication of Circular Channel Microfluidic Flow-Focusing Devices for Hydrogel Droplet Generation," *Nano-Micro Letters* 11 (2016): 41–45, https://doi.org/10.1049/mnl.2015.0329.

25. M. G. A. Mohamed, S. Kheiri, S. Islam, H. Kumar, A. Yang, and K. Kim, "An Integrated Microfluidic Flow-Focusing Platform for On-Chip Fabrication and Filtration of Cell-Laden Microgels," *Lab on A Chip* 19 (2019): 1621–1632, https://doi.org/10.1039/C9LC00073A.

26. A. Fergola, C. G. Gaglio, S. L. Marasso, et al., "Biomaterials in Droplet-Based Microfluidics: From Structural Design to Biomedical Applications," *Materials Today Advances* 28 (2025): 100667, https://doi.org/10.1016/j.mtadv.2025.100667.

27. X. Chen, D. Zhang, X. Wang, et al., "Preparation of Porous GelMA Microcarriers by Microfluidic Technology for Stem-Cell Culture," *Chemical Engineering Journal* 477 (2023): 146444, https://doi.org/10.1016/j.cej.2023.146444.

28. T. Liu, W. Weng, Y. Zhang, X. Sun, and H. Yang, "Applications of Gelatin Methacryloyl (GelMA) Hydrogels in Microfluidic Technique-Assisted Tissue Engineering," *Molecules* 25 (2020): 5305, https://doi.org/10.3390/molecules25225305.

29. H. Wang, H. Liu, H. Liu, W. Su, W. Chen, and J. Qin, "One-Step Generation of Core–Shell Gelatin Methacrylate (GelMA) Microgels Using a Droplet Microfluidic System," *Advanced Materials Technologies* 4 (2019): 1800632, https://doi.org/10.1002/admt.201800632.

30. Y. Wang, T. Du, X. Hao, et al., "Microfluidic Droplet-Based Tailorable Porous GelMA Microspheres for 3D Spatio Controllable Cell Coculture," *Advanced Materials Technologies* 9 (2024): 2301697, https://doi.org/10.1002/admt.202301697.

31. H. Bruus, *Theoretical Microfluidics*, Vol. 18. Oxford university press 2007.

32. J. Park, S. Park, K. A. Hyun, and H.-I. Jung, "Microfluidic Recapitulation of Circulating Tumor Cell–Neutrophil Clusters via Double Spiral Channel-Induced Deterministic Encapsulation," *Lab on A Chip* 21 (2021): 3483–3497, https://doi.org/10.1039/D1LC00433F.

33. T. Tang, H. Zhao, S. Shen, L. Yang, and C. T. Lim, "Enhancing Single-Cell Encapsulation in Droplet Microfluidics With Fine-Tunable on-Chip Sample Enrichment," *Microsyst Nanoeng* 10 (2024): 3, https://doi.org/10.1038/s41378-023-00631-y.

34. M. Vigata, C. Meinert, N. Bock, B. L. Dargaville, and D. W. Hutmacher, "Deciphering the Molecular Mechanism of Water Interaction With Gelatin Methacryloyl Hydrogels: Role of Ionic Strength, PH, Drug Loading and Hydrogel Network Characteristics," *Biomedicines* 9 (2021): 574, https://doi.org/10.3390/biomedicines9050574.

35. D. Grijalva Garces, C. P. Radtke, and J. Hubbuch, "A Novel Approach for the Manufacturing of Gelatin-Methacryloyl," *Polymers (Basel)* 14 (2022): 5424, https://doi.org/10.3390/polym14245424.

36. C. G. Gaglio, D. Baruffaldi, C. F. Pirri, L. Napione, and F. Frascella, "GelMA Synthesis and Sources Comparison for 3D Multimaterial Bioprinting," *Frontiers in Bioengineering and Biotechnology* 12 (2024): 1383010, https://doi.org/10.3389/fbioe.2024.1383010.

37. B. Büyükurgancı, S. K. Basu, M. Neuner, J. Guck, A. Wierschem, and F. Reichel, "Shear Rheology of Methyl Cellulose Based Solutions for Cell Mechanical Measurements at High Shear Rates," *Soft Matter* 19, no. 9, (2023): 1739–1748.

38. A. I. Van Den Bulcke, B. Bogdanov, N. De Rooze, E. H. Schacht, M. Cornelissen, and H. Berghmans, "Structural and Rheological Properties of Methacrylamide Modified Gelatin Hydrogels," *Biomacromolecules* 1 (2000): 31–38, https://doi.org/10.1021/bm990017d.

39. B. H. Lee, H. Shirahama, N.-J. Cho, and L. P. Tan, "Efficient and Controllable Synthesis of Highly Substituted Gelatin Methacrylamide for Mechanically Stiff Hydrogels," *RSC Advances* 5 (2015): 106094–106097, https://doi.org/10.1039/C5RA22028A.

Supporting Information

Additional supporting information can be found online in the Supporting Information section.

Supporting File 1: admt71181-sup-0001-SuppMat.docx.